

# Exploring the Inhomogeneous Nature of Li Intercalation and Li Plating on Graphite Anodes—An Experimental Study Combining Inert Gas High-Resolution Light Microscopy with Colorimetric and Machine Learning-Based Image Analysis

Marius Bolsinger, Christian Weisenberger,\* Thomas Waldmann, Marc Kamlah, and Volker Knoblauch

Li plating significantly contributes to the ageing of lithium-ion batteries (LIBs). An in-depth understanding of Li-ion intercalation kinetics into graphite, still being widely used as anode material, and the subsequent phase formation of  $\text{Li}_x\text{C}_6$  compounds, is necessary to understand kinetic limits and prevent Li plating. Diffraction and colorimetric studies have explored these processes, noting graphite color changes during (de)intercalation. However, these methods fall short of examining graphite intercalation at a microscopic scale, essential for understanding intercalation kinetics and Li plating onset conditions. This study employs a high-resolution light microscope under inert gas to examine lithiation processes in graphite anodes at the particle level across various C-rates. Qualitative descriptions and quantitative assessments are achieved through colorimetric analysis based on hue and saturation, complemented by machine learning-based segmentation. The results show an increased spatial heterogeneity of lithiation stages both between particles and within individual particles, with increasing C-rate. Notably, up to three stages coexist in one particle, and  $\text{LiC}_6$  is present at 50% (SOC) state of charge even when lithiated with 0.2C. At 1C charging, 4% and 32.5% of the surface is covered with Li deposits at 30% and 50% SOC, respectively, with underlying graphite particles showing  $\text{LiC}_6$ .

material for LIBs inter alia due to its high-capacity retention, relatively low volume expansion upon lithiation, low cost, and low toxicity. Lithium plating is one of the main ageing mechanisms in LIBs<sup>[2]</sup> and affects many key cell properties that are relevant for the cell's application. It causes capacity loss and a reduced coulombic efficiency due to loss of Li inventory and electrolyte consumption<sup>[3]</sup> as well as power fade due to a rise in the internal resistance.<sup>[4]</sup> In addition, it can cause safety issues due to gas evolution, internal electrical shorting and might also increase the risk of thermal runaway.<sup>[5–7]</sup> Li plating is directly linked to the intercalation process of Li-ions into graphite, as Li plating occurs when intercalation is stoichiometrically or kinetically limited or even not possible. To understand and prevent Li plating, a profound understanding of the Li intercalation, distribution, and plating processes on a microscopic scale is necessary.<sup>[8–11]</sup> Understanding ageing mechanisms can help to prevent them, leading to enhanced battery life and therefore to


## 1. Introduction

Li-ion batteries (LIBs) are widely used as energy storage in portable electronics, electromobility, and stationary energy storage systems.<sup>[1]</sup> Graphite is the common choice for negative electrode

increased sustainability and less dependency on critical resources.

During charging, Li-ions intercalate between the graphene layers of graphite, forming lithium-graphite intercalation compounds (GICs) with different lithiation stages. The intercalation stage refers to the number of graphene layers between two

M. Bolsinger, C. Weisenberger, V. Knoblauch  
Materials Research Institute Aalen (IMFAA)  
Aalen University of Applied Sciences  
Beethovenstraße 1, D-73430 Aalen, Germany  
E-mail: christian.weisenberger@hs-aalen.de

 The ORCID identification number(s) for the author(s) of this article can be found under <https://doi.org/10.1002/aesr.202500181>.

© 2025 The Author(s). Advanced Energy and Sustainability Research published by Wiley-VCH GmbH. This is an open access article under the terms of the Creative Commons Attribution License, which permits use, distribution and reproduction in any medium, provided the original work is properly cited.

DOI: 10.1002/aesr.202500181

T. Waldmann  
Zentrum für Sonnenenergie- und Wasserstoff-Forschung  
Baden-Württemberg (ZSW)  
Lise-Meitner-Straße 24, D-89081 Ulm, Germany

T. Waldmann  
Helmholtz Institute Ulm for Electrochemical Energy Storage (HIU)  
Helmholtzstrasse 11, D-89081 Ulm, Germany

M. Kamlah  
Institute for Applied Materials - Mechanics of Materials and Interfaces (IAM-MMI)  
Karlsruhe Institute of Technology (KIT)  
Hermann-von-Helmholtz-Platz 1, D-76344 Eggenstein-Leopoldshafen, Germany

adjacent, Li-intercalated layers stacked in a periodic fashion.<sup>[12]</sup> Beginning at low Li-concentrations with the dilute Stages 1L, 4L, 3L, and 2L (LiC<sub>18</sub>) to the ordered stages 2 (LiC<sub>12</sub>) and finally 1 (LiC<sub>6</sub>).<sup>[13]</sup> This phenomenon has been intensively investigated by means of X-ray<sup>[12,14]</sup> and neutron diffraction<sup>[15–17]</sup> and Raman spectroscopy.<sup>[18,19]</sup>

In addition, the lithium intercalation compounds can also be distinguished visually as the graphite undergoes a significant color change during intercalation, with stage 1 (LiC<sub>6</sub>) appearing golden, stage 2 (LiC<sub>12</sub>) red, and stage 2L (LiC<sub>18</sub>) blue.<sup>[20–23]</sup> The observed color change is well understood and results from the absorption of photons at specific wavelengths known as the Drude edge.<sup>[24,25]</sup> This enables the use of optical microscopy to reveal important aspects of the kinetics of graphite lithiation with high local resolution.

Maire et al.<sup>[26,27]</sup> developed in situ colorimetry to measure the local SOC of a lithiated graphite electrode by measuring its color on a millimeter scale and showed that the Li distribution in anodes of aged LIBs is highly heterogeneous. Harris et al.<sup>[28,29]</sup> published a direct in situ time-dependent measurement of Li transport in an operating Li-ion cell and transport rate measurements at the mesoscale. Gyenes et al.<sup>[30]</sup> showed, based on time-dependent color gradients, lateral redistribution to the overhang areas of the graphite anode. Grimsman et al.<sup>[31]</sup> report that there are color differences at the same state of charge, depending on the charge and discharge direction, and a current dependency with colors that do not correspond to the average state of charge of the graphite anode. Hogrefe et al.<sup>[32,33]</sup> developed an in situ microscopy cell for time-resolved observation of color changes in cross-sectioned Li-ion full cells and showed that colored lithiation fronts of LiC<sub>12</sub> and LiC<sub>6</sub> are moving through the anode from the separator to the current collector during charging.

Many studies use digital cameras and stereomicroscopes for the optical investigations on a more macroscopic scale, and therefore lack information on the particle level. In situ optical measurements are a valuable instrument to enable the observation of Li distribution within graphite on a particle level.<sup>[32,34–40]</sup> However, operando and in situ optical measurements are still significantly limited in resolution, as the working distance is increased by a glass window that protects the cell. In addition, operando optical techniques often apply a less application-oriented setup with electrodes placed side by side or thin electrodes observed from the back through a sealed hole in the cell and current collector.<sup>[34,36]</sup> Such set-ups may affect the electrochemical processes within these cells and thus, the observed lithiation and plating processes. Furthermore, optical investigations of lithiation and Li plating are challenging due to their high reactivity and sensitivity to oxygen and moisture, leading to rapid degradation of the material, especially on the surface, and inaccurate experimental results.<sup>[41]</sup>

Besides a qualitative description of the color change, the high-resolution images that have been acquired with this setup also allow a quantitative analysis of the lithiation process, either by means of colorimetric analysis or phase segmentation. As described above, colorimetric analysis was applied to identify the degree of lithiation in graphite anodes by Maire et al.<sup>[26]</sup> and Grimsman et al.<sup>[31]</sup> by analyzing the values for the red, green, and blue (RGB) channels of the images. However, using RGB values has the problem that the color information is ‘hidden’

within the ratio of all three channels, which can be less intuitive and sometimes misleading, as a color shift can influence the RGB values in either way. In a recent publication, Jansche et al.<sup>[35]</sup> used a rather advanced approach by calculating pixel-based parameters for colorfulness from images acquired with an in situ light optical microscope<sup>[32]</sup> to estimate the degree of lithiation of graphite anodes.

Phase segmentation and quantitative analysis are even more challenging. Because of the sample topography, “classical” threshold-based methods cannot be used as they call for a distinct phase contrast and color values with low deviation for each phase.

To overcome the above-mentioned issues, our approach utilizes a novel test setup and techniques for colorimetric analysis and phase segmentation.

Instead of utilizing operando test cells with optical windows, we installed a remotely controlled high-resolution light microscope directly into an Ar-filled glovebox. This brings several advantages: First, the lack of an optical window allows us to use high-end color-corrected objectives with a very high numerical aperture of up to 0.9 and a theoretical resolution of 0.305 μm to resolve the graphite particles in detail. To the best of our knowledge, we are the first to use such a high-resolution light microscope under an inert gas atmosphere to investigate lithiation and plating processes in graphite anodes that have been subjected to various charging conditions. In addition, as we did not perform operando tests but “interrupted” charging tests, we were able to use standard coin cells without further modifications that might have a negative effect on the electrochemical conditions in the cell and graphite electrodes with compositions and microstructures relevant for industrial applications.

To overcome the issues related to RGB colorimetry, we applied a colorimetric analysis based on the hue, saturation, and luminance (HSL) color space using the hue and saturation values of the images. The advantage of this method is that the color impression that corresponds to the lithiation stages is represented by a single value (hue), whereas the saturation indicates how colorful the image is. In addition, this technique is simple and can easily be reproduced with most image processing software.

For quantitative image analysis and image segmentation, we use machine learning (ML) based semantic segmentation to quantify changes of phase fractions (LiC<sub>18</sub>, LiC<sub>12</sub>, and LiC<sub>6</sub>) as well as Li depositions. This ML-based approach uses convolutional neural networks or random forest techniques<sup>[42,43]</sup> to distinguish between the phases. It has already been applied to battery electrodes to differentiate pores and active materials in tomographic datasets.<sup>[44,45]</sup> In this work, graphite anodes were studied at different C-rates.

With our approach, we were able to reveal the formation of intercalation phases with high spatial resolution and describe the phase distributions qualitatively and quantitatively. In addition, we could demonstrate the feasibility of ML-based phase segmentation using images with high sample topography. In doing so, this study provides new insights onto the inhomogeneous nature of Li intercalation processes and Li plating in graphite-based anodes and how the SOC and C-rate influence them.

## 2. Results and Discussion

### 2.1. Lithiation and Color Change of the Graphite Anode during 0.1C Charge

To study the lithiation process and color change at low C-rates, multiple cells were charged in CC mode with 0.1C to the desired SOC from 0%–100% and then disassembled. Prior to performing the in-depth microscopic analysis, we combined the data from the voltage curve, macro images, and X-ray diffraction analysis to ensure that our samples are lithiated homogeneously and that the crystallographic phases we would expect from the voltage curves are actually present in the sample (Figure 1).

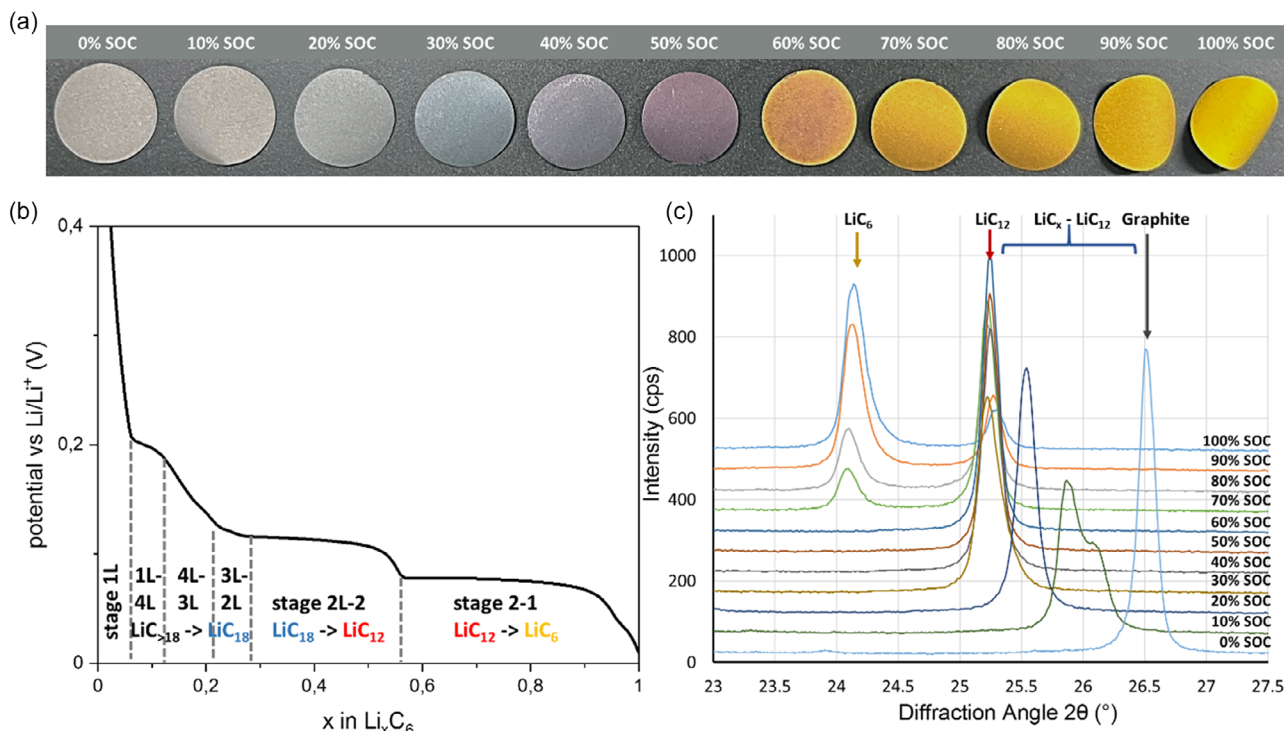
As seen in Figure 1b we observe the typical voltage profile described in the literature<sup>[12,13]</sup> with steps in the voltage profile indicating single-phase regions, whereas plateaus indicate two-phase regions with a transformation from one phase to another. These plateaus are particularly pronounced for the formation of  $\text{LiC}_{12}$  between 30% SOC and 60% SOC and the formation of  $\text{LiC}_6$  between 60% SOC and 100% SOC. The stages that can be identified in the voltage profile are in good agreement with the color change that can be observed in the macroscopic images. However, the macroscopic images are only intended to give a first impression and will not be discussed further at this point. In the diffraction patterns (Figure 1c), the graphite peak is clearly visible at  $\approx 26.5^\circ$  ( $2\theta$ ) for the 0% SOC sample and disappears at 10% SOC. For 10% SOC and 20% SOC, we clearly observe diffraction peaks for the dilute stages ( $\text{LiC}_x$  with  $x > 12$ ). Between

10% SOC and 30% SOC, the d-spacing of the dilute phases gradually approaches that of  $\text{LiC}_{12}$ .<sup>[46]</sup>

At 30% SOC (Figure 1b)  $x = 0.3$  in  $\text{Li}_x\text{C}_6$  we observe the beginning of the transition from the dilute stage 2L ( $\text{LiC}_{18}$ ) to ordered stage 2 ( $\text{LiC}_{12}$ ). At this point, we can only see a peak at the position associated with the  $\text{LiC}_{12}$  phase at  $\approx 25.25^\circ$   $2\theta$ , which increases in intensity until it reaches its maximum at 60% SOC. This clearly indicates an increase in the amount of the  $\text{LiC}_{12}$  phase between 30% and 60% SOC, which is in good agreement with the voltage profile. The data obtained by Yao et al. with operando energy dispersive X-ray diffraction (XRD) shows that the peak intensity for the 2L stage quickly drops between 20% and 30% SOC, and that at 30% SOC, the peak intensity for the  $\text{LiC}_{12}$  peak is lower than that of the stage 2L peak at 20% SOC.<sup>[46]</sup> This is exactly what we observe, and thus, we can assume that the dilute stages are still present, yet not visible as separate peaks due to the increasing crystallographic similarity with  $\text{LiC}_{12}$ .

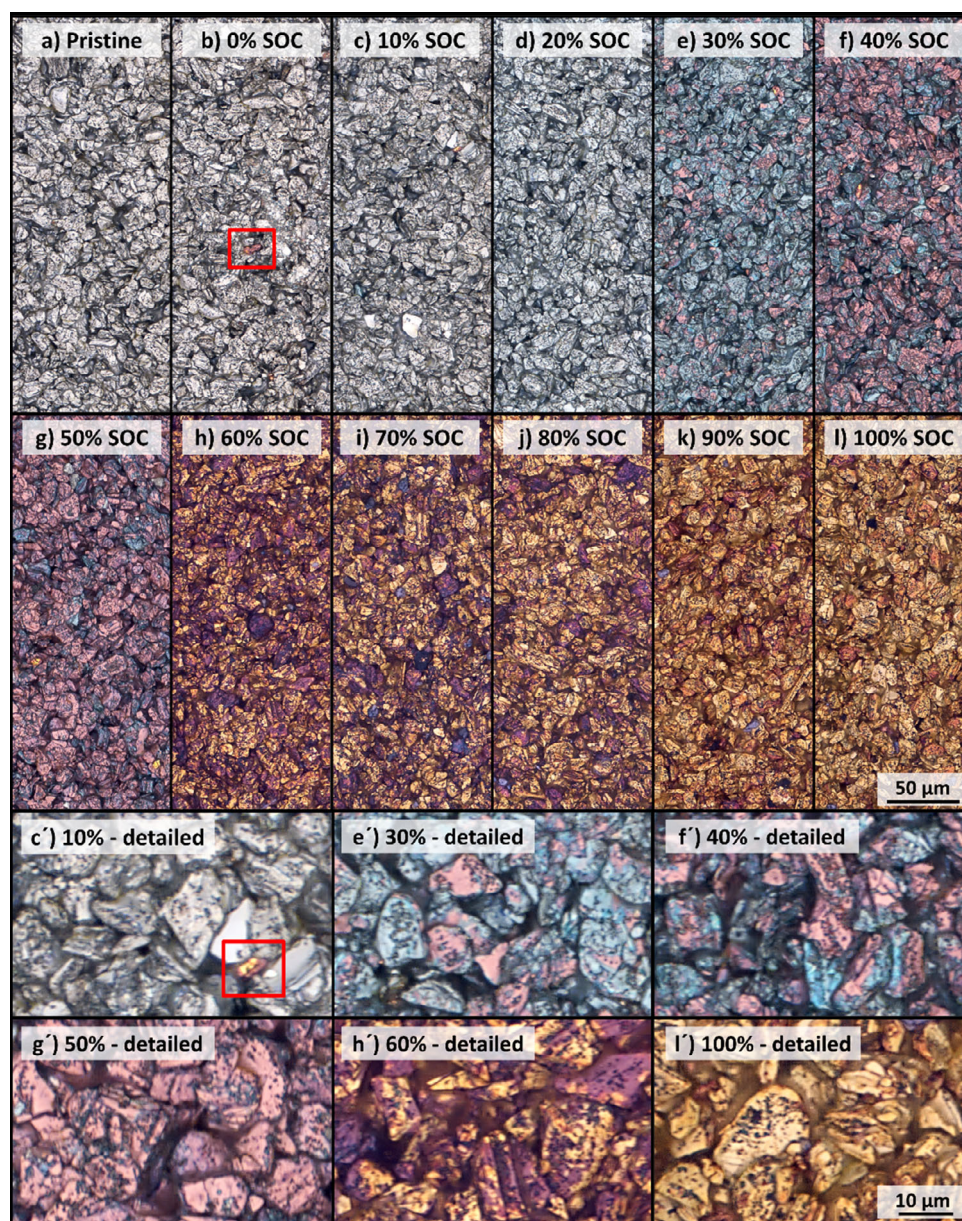
From 60% SOC to 100% SOC, phase transformation from  $\text{LiC}_{12}$  into  $\text{LiC}_6$  takes place, and peak intensity for the  $\text{LiC}_{12}$  peak decreases, whereas the peak intensity for the  $\text{LiC}_6$  peak (at  $24.1^\circ$   $2\theta$ ) increases, reaching its maximum at 100% SOC. After verifying the phases by means of XRD, high-resolution light optical microscopy was performed.

Figure 2a-l shows the microscope images of the anode surfaces from 0% to 100% SOC in 10% SOC steps, demonstrating the color changes from gray (unlithiated graphite), through blue ( $\text{LiC}_{18}$ ) and red ( $\text{LiC}_{12}$ ), to gold ( $\text{LiC}_6$ ). Again, the color change



**Figure 1.** Correlation between color, electrode potential and the crystallographic phases of graphite anodes: a) macro images of electrodes, b) cell potential versus  $\text{Li/Li}^+$  with corresponding SOC for XRD measurements, c) diffraction patterns from XRD measurements at different SOC between  $23^\circ$  and  $27.5^\circ$  ( $2\theta$ ) showing the peaks for graphite, the dilute stages ( $\text{LiC}_x$  with  $x > 12$ ),  $\text{LiC}_{12}$ , and  $\text{LiC}_6$  (right).





**Figure 2.** Light microscope images of the graphite anode surfaces: a) pristine before building into the cell, b-l') after cell opening and washing in DMC from 0% to 100% SOC in 10% SOC steps, showing color changes from gray (unlithiated graphite), through blue ( $\text{LiC}_{18}$ ) and red ( $\text{LiC}_{12}$ ) to gold ( $\text{LiC}_6$ ). c', e'-h', l') are high magnifications of (c, e-h, l) respectively.

is in good agreement with our XRD measurements and observations from the literature.<sup>[21,31]</sup>

Upon closer examination, we can extract more details on the particle and sub-particle level. The surfaces of the pristine graphite anode (Figure 2a), the 0% SOC sample after formation (Figure 2b), and the anode charged to 10% (Figure 2c) are homogeneously gray in color. The intercalation of a small amount of Li ( $x < 0.2$ , in  $\text{Li}_x\text{C}_6$ ) has little effect on the color. In Figure 2b and Figure 2c', small graphite particles with a red or red-gold coloring, indicating higher stages of lithiation ( $\text{LiC}_{12}$  and  $\text{LiC}_6$ ), can occasionally be observed on the surface. As the electrodes have undergone a formation process prior to

charging them to a specific SOC, the color of these particles can be explained by the loss of electrical contact during the previous charging or discharging process. Similar disconnected particles with a different lithiation degree in a different graphite anode coating were also observed by Hogrefe et al.<sup>[32]</sup>

A first visual change of the entire surface can be observed at 20% SOC (Figure 2d), where the electrode surface turns slightly blue, indicating the presence of  $\text{LiC}_{18}$ , which is well in line with the finding of the stage 2L peak in the XRD data. This blue coloration of the surface and within individual particles becomes significantly stronger at 30% SoC (Figure 2e) and can also be



recognized to a small extent in the images taken with the digital camera (Figure 1a).

At 30% SOC, several particles possess two colors—the blue indicating  $\text{LiC}_{18}$  and a pink reddish color, indicating  $\text{LiC}_{12}$  (Figure 2e'). Note that there are some completely pink particles (Figure 2e'), which in turn is consistent with the first appearance of the XRD peak at  $25.25^\circ$  ( $2\theta$ ). 30% SOC marks the start of the two-phase transition (stage 2L-2). This explains why the blue of  $\text{LiC}_{18}$  is still the predominant color. Two colored particles indicate different lithiation states within one particle, which was also shown by Migge et al. via Raman spectroscopy<sup>[18]</sup> and by Hogrefe et al. via in situ optical microscopy.<sup>[32]</sup> It becomes obvious that Li intercalation does not proceed homogeneously over the graphite anode surface even at a comparatively low C-rate of 0.1C.

A spatial nonuniformity can be observed starting at 30% SOC, which is well in line with the study of Panitz et al. investigating the lithiation of polycrystalline graphite.<sup>[19]</sup> The solid solution of the dilute stages (1L-4L) prevents noticeable phase separations and leads to a homogeneous appearance.<sup>[36]</sup> At 30% SOC, the stoichiometric phases  $\text{LiC}_{18}$  and  $\text{LiC}_{12}$  can be distinguished, and the lithiation tends to start in particles or areas with a, for example, favorable crystallite orientation.<sup>[47–49]</sup> Other reasons for spatial variation are tortuosity, electrical contact resistance, and/or solid electrolyte interphase (SEI) film resistance and crystallographic misfits.<sup>[18,34,50–52]</sup>

With further lithiation to 40% SOC, the graphite surface shows an increasingly stronger red/pink coloration, and the blue component decreases obviously (Figure 2f,f'). At 50% SOC, we find mainly pink particles that only have punctual blue areas (Figure 2g,g'). The color changes observed are in line with the findings of the XRD results, where an increase in the  $\text{LiC}_{12}$  peak was detected, and the voltage curve indicates a near end of the 2L to 2 transition. However, the color impression obtained from the microscopic images is more differentiated than the XRD, as a gradual transition from blue to red can be seen between 30% and 50% SOC—while no  $\text{LiC}_{18}$  phase is detected in the XRD anymore.

At 60% the transition from stage 2 to stage 1 has already started, manifested in a red and golden ( $\text{LiC}_6$ ) anode surface, and many of the individual particles start to turn golden (Figure 2h,h'). Again, there are rarely monochromatic particles, i.e., most of the particles exhibit different GICs at the same time. It seems that intercalation starts at various interfaces, and there is no visible preferential surface structure for preferred intercalation. In contrast, the XRD measurements at 60% SOC do not reveal a  $\text{LiC}_6$  peak. We assume that the formation of  $\text{LiC}_6$  on the electrode surface has already begun, but to such a small extent that the resolution of the XRD is not sufficient to detect this. A stronger lithiation of the anode surface during charging is consistent with in situ optical microscopy measurements of cross-sectioned full cells<sup>[32,33,53]</sup> and with simulations.<sup>[54–56]</sup>

As the SOC continues to increase, the  $\text{LiC}_{12}$  phase continues to decrease, while the proportion of  $\text{LiC}_6$  is increasing, which also fits well with our XRD results. Above 90% SOC, the  $\text{LiC}_{12}$  phase is present only very sporadically (Figure 2k). At 100% SOC, we basically observe only completely lithiated particles (Figure 2l,l'), and the XRD-plot reveals a maximum of the  $\text{LiC}_6$  peak (at  $24.1^\circ$   $2\theta$ ). The small  $\text{LiC}_{12}$  peak originates likely from areas close to the current collector that have not yet been completely lithiated.

To summarize, the high-resolution microscope under an inert gas atmosphere enables the optical examination of charged graphite anodes at a microscopic scale to gain a deeper understanding of the lithiation processes. In addition to the color changes that an anode undergoes, it can be shown that the different lithiation stages are coexisting and visible even within one particle at a low C-rate.

## 2.2. Influence of the C-rate on the Lithiation of a Graphite Anode

To study the lithiation process and color change at higher C-rates, a minimum of three cells were charged in CC mode with various C-rates (0.1C; 0.2C; 0.33C; 0.5C; 1C) to 30% and 50% SOC, afterward disassembled and microscopically investigated (Figure 3). The corresponding voltage curves can be found in the supplementary data (Figure S1, Supporting Information).

### 2.2.1. 30% SOC

The increase in the C-rate leads to a clear color change on the anode surface and within individual particles. Already at a C-rate of 0.2C (Figure 2c), the anode surface appears significantly redder compared to the 0.1C reference (Figure 2a), thus indicating a higher proportion of the  $\text{LiC}_{12}$  phase. This effect becomes increasingly pronounced at 0.33C (Figure 2e) and 0.5C (Figure 2g). Increasing the C-rate leads to a more inhomogeneous Li intercalation and a fast saturation at the surface of the anode with Li-ions, thus resulting in a gradient across the graphite anode and within the graphite particles.<sup>[17,32,57,58]</sup> At 0.5C the potential falls below 0 V (Figure S1, Supporting Information), but without showing any visual signs of plating, and Li-intercalation appears to be the predominant mechanism. After charging with 1C, some gold-colored particles appear, and Li deposition can be confirmed visually (Figure 3i,i'). Even though the potential is significantly below 0 V (see supplementary data Figure S1, Supporting Information), the lithium deposition is only local, as also observed by Ref.<sup>[39]</sup> This deposited Li appears white, with an often needle-type structure, as also observed with optical confocal microscopy by Uhlmann et al.<sup>[59]</sup> As described by Ref.<sup>[60]</sup> Li deposition occurs when the Li-ion current in the electrolyte exceeds the intercalation current or the transport rate through solid diffusion. In consequence, the anode potential drops below the potential of metallic Li deposition due to the involved overpotentials, i.e., charge-transfer and diffusion overpotentials.<sup>[61,62]</sup>

Lithium appears to be predominantly deposited on the fully lithiated (golden-yellow) regions of the graphite particles (Figure 3i') as they favor nuclei for Li deposition as proposed by Gao et al.<sup>[38]</sup> and Chen et al.<sup>[63]</sup> Occasionally, some depositions can be found in darker areas. Note that with our method, we only gain a top view of the electrode. It is possible that a small region of  $\text{LiC}_6$  lies directly underneath the depositions or that the depositions have grown into the darker regions. Even after an immediate transfer to the glovebox after charging, it might also be possible that the deposited Li re-intercalates during this time. Hogrefe et al. presented a systematic study on the Li transport pathways in the reaction of Li metal with a graphite electrode. They showed that the re-intercalation of electrically connected

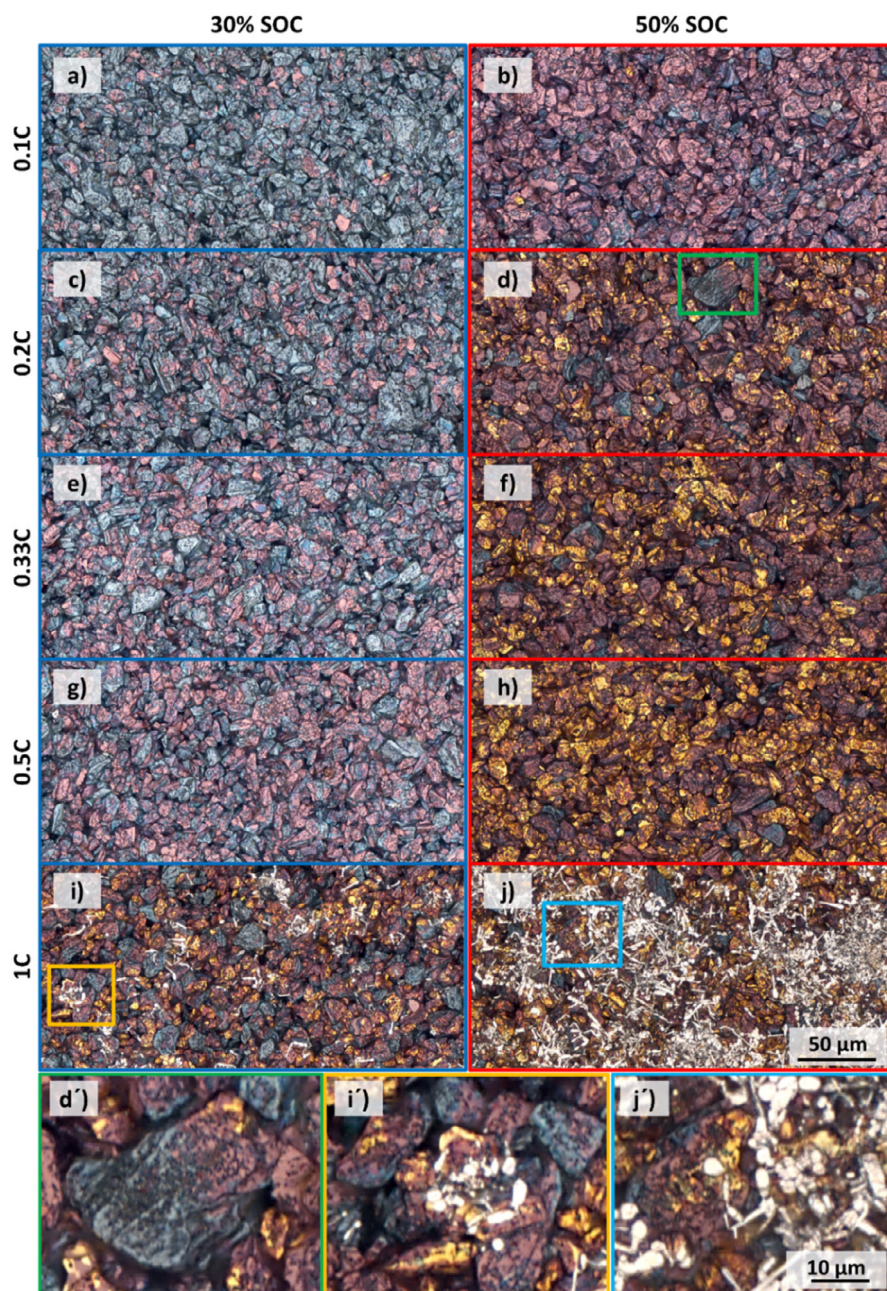


**Figure 3.** Light microscopy images of the graphite anode surfaces after cell opening and washing in DMC. Anodes were charged to 30% SOC (a,c,e,g,i, blue frames) and 50% SOC (b,d,f,h,j, red frames) with increasing C-rate from 0.1C (first row) to 1C (second last row). Images in the lowest row show enlargements of the color-marked areas: d') – green. i') – orange. j') – turquoise.

Li is possible even in dried areas and that this can increase the degree of lithiation of the graphite particles near the local Li plating.<sup>[64]</sup>

### 2.2.2. 50% SOC

Charging to 50% SOC, the increase of the C-rate leads to an even more pronounced color change of the anode surface and within individual particles. The effects and correlations described above for 30% SOC are in principle the same but even more

pronounced. While at 0.1C most of the particles are pink ( $\text{LiC}_{12}$ ) and there is nearly no  $\text{LiC}_6$  phase (Figure 3b), at higher C-rates the degree of intercalation shows again significant differences from particle to particle and even on the surface of specific particles, i.e., at 0.2C there are several yellow or at least yellow dotted particles (Figure 3d). For example, one specific particle (Figure 3d') shows the co-existence of the blue, red, and golden phases, which can also be seen in the samples charged to 30% SOC in Figure 3i' and Figure 3j'. This phase separation has been reported by several in situ optical studies<sup>[36–38]</sup> but is resolved in



much more detail here. The results of Agrawal and Bai<sup>[36]</sup> indicate only two coexisting phases. Gao et al.<sup>[38]</sup> also observed three phases, however, in a considerably larger particle of highly oriented pyrolytic graphite.

The phase separation is present in both larger and smaller particles, which is consistent with the optical observations made by Agrawal and Bai.<sup>[36]</sup> Basal plane orientation is often discussed in relation to graphite lithiation.<sup>[65–68]</sup> Judging by the visual appearance of the surface morphology and color of the

particles, it seems that the lithiation starts at a particle's edge, with phase separation fronts running perpendicular to the basal planes of the particle. However, commercial graphites are usually rounded to some degree,<sup>[69]</sup> making it difficult to determine the crystallographic orientation of the graphite surface. It can be expected that after calendaring, the graphite basal planes are to a high degree oriented parallel to the current collector surface.<sup>[70]</sup> Migge et al.<sup>[18]</sup> observed a three-phase separation with Raman spectroscopy and pointed out that the intercalation

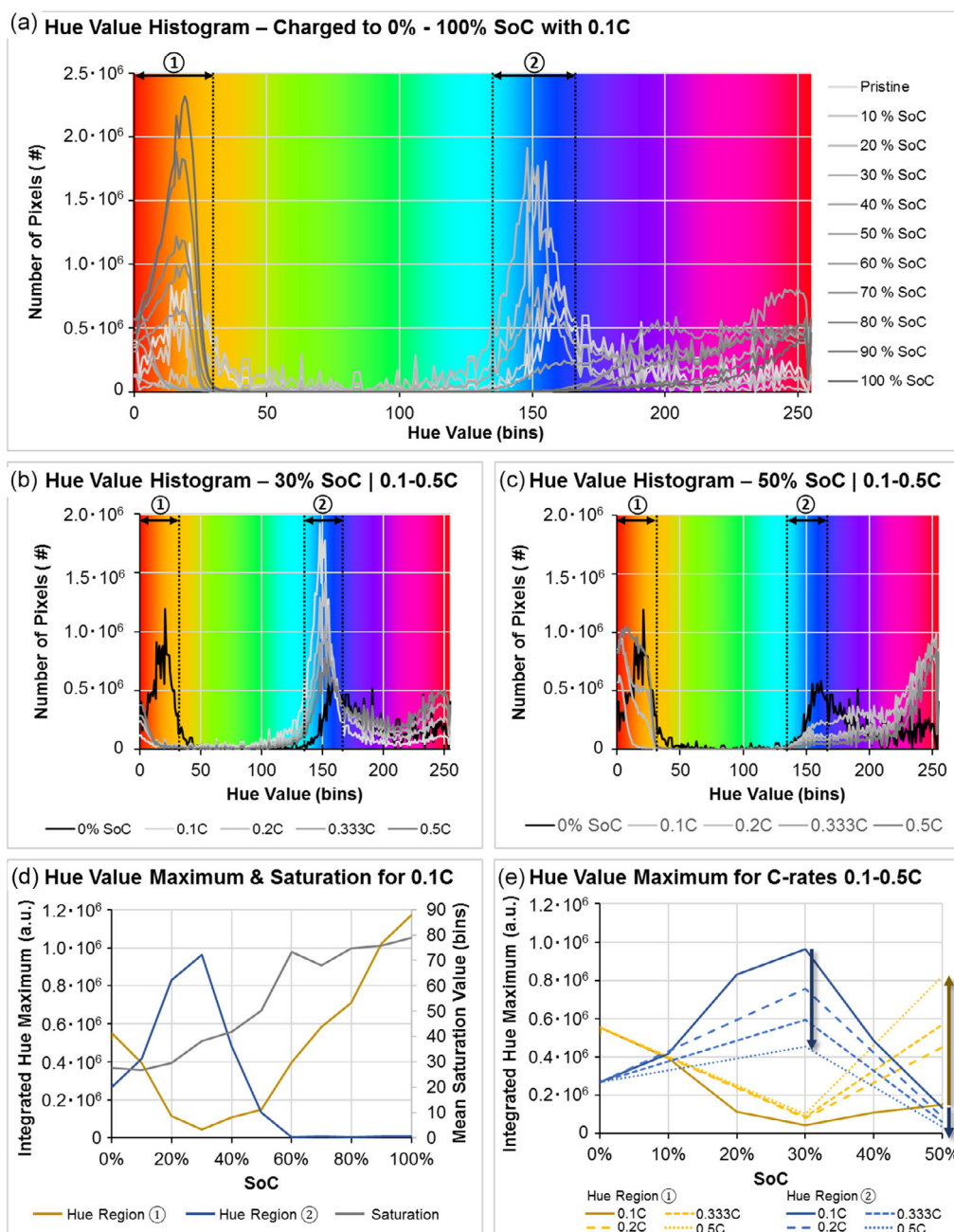


**Figure 4.** Colorimetric analysis of microscopy images. a) Hue value histogram of specimens charged to 0%–100% SOC (see Figure 2) with 0.1C showing the distinctive regions ① and ②. b,c) Hue value histograms of specimens charged to (b) 30% SOC and to (c) 50% SOC with different C-rates (see Figure 3). d) Extracted Hue value maxima for regions ① and ② and saturation value from samples shown in (a). e) Extracted Hue value maxima for values from histograms shown in (b) and (c).

starts at the parts of the particle pointing toward the electrolyte reservoir.

When charged to 50% SOC with 1C, the appearance of the lithium dispositions changes from the local spots to a layer with a grainy and dendritic structure, as observed by Ref. [71–73], covering whole regions (Figure 3j). Besides the visual confirmation, we applied energy-dispersive X-ray spectroscopy (EDS) with a windowless detector and laser-induced breakdown spectroscopy (LIBS) to confirm that the observed structures are lithium depositions (Figure S2, Figure S3, Supporting Information). There is clearly more Li deposition than on the anode that was charged to 30% at the same C-rate.

The observation made shows a clear correlation between SOC, C-rate, and amount of plating, and 1C was identified as the critical C-rate for lithium plating. However, it has to be noted that these observations are only valid for the given test conditions. Considering fast charging, the temperature is an important factor.<sup>[39,74,75]</sup> Changing the temperature to lower values would most probably lead to a more severe plating at lower SOC

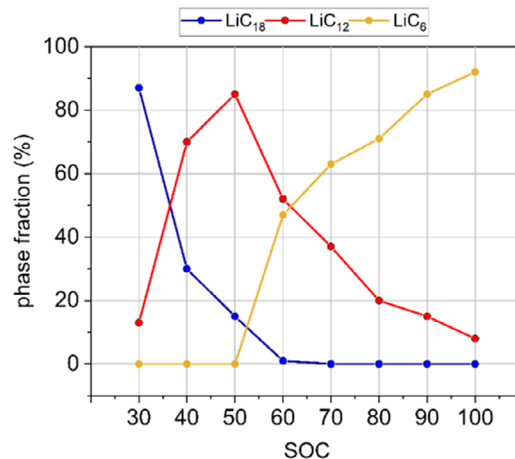
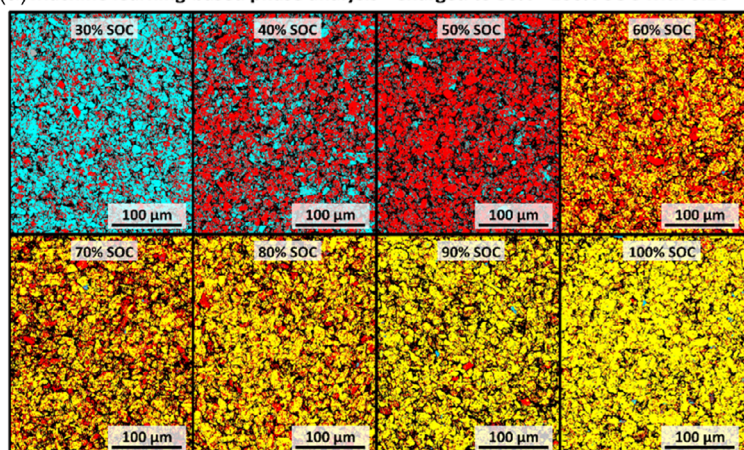
and C-rates.<sup>[39,40,75,76]</sup> In addition, the choice of the electrolyte (and its additives) is curtail and can successfully prevent or even facilitate plating in a LIB.<sup>[77,78]</sup>

### 2.3. Quantification of Lithiation and Li Plating Using Colorimetric Analysis and ML-Based Phase Analysis

In Figure 4a, the histograms for the hue value from electrode images charged from 0% SOC to 100% SOC with 0.1C are plotted (original images shown in Figure 2).

We can basically identify two regions in the histogram with distinct peaks. One between a hue value of 0 and 30 region ① representing an orange–yellow color, and one between a hue value of 135 and 165 region ② representing a blueish color. The integrated intensities for both regions are plotted in Figure 4d together with the mean value for saturation. At 0% SOC, both peaks are of similar intensity with a low saturation value, indicating a grayish color of the sample. The saturation value increases constantly during lithiation, indicating that the image

(a) Machine learning-based phase analysis - Charged to 30% - 100% SOC with 0.1C



(b) Machine learning-based phase analysis - Charged to 30% and 50% SOC with 0.1C – 0.5C

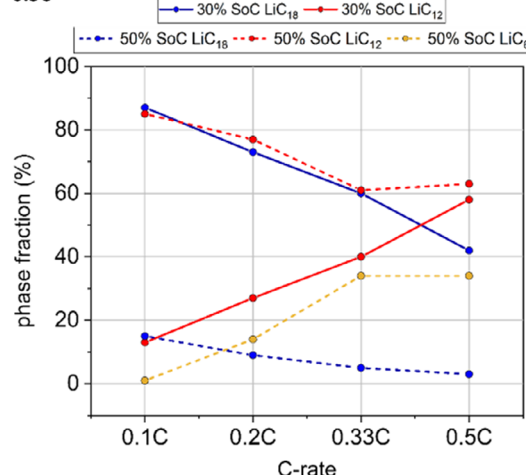
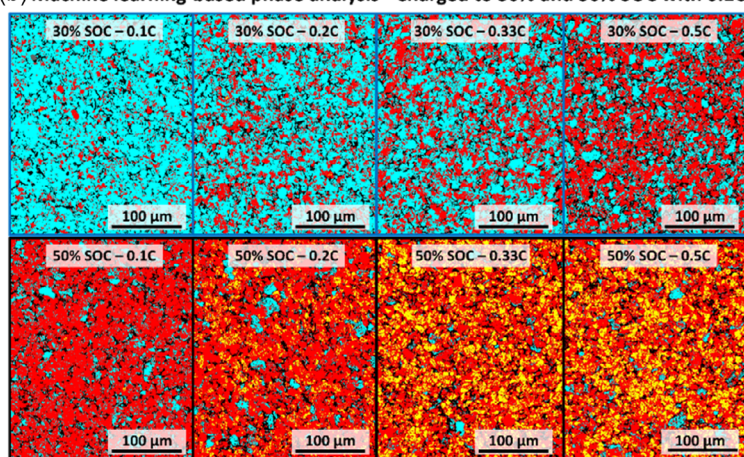


**Figure 5.** ML-based phase analysis using ZEN Intellesis of microscopy images. Left: Segmented microscopy images of the graphite anode surfaces. The anodes were charged to 30% SOC a) and 50% SOC b) with an increase in the C-rate from 0.1C (first column) to 0.5C (last column). On a particle level, a good separation of LiC<sub>18</sub> (blue), LiC<sub>12</sub> (red), LiC<sub>6</sub> (yellow), and porosity (black) is possible. Right: Quantification of LiC<sub>x</sub> phase fractions using ML-based segmentation.



becomes more colorful. Between 0% SOC and 30% SOC, the samples shift their color toward blue; hence, the intensity of region ② increases, whereas the intensity of region ① decreases. Between 30% SOC and 100% SOC, we observe the opposite trend, representing a color shift toward the golden–yellow color of  $\text{LiC}_6$ . For  $\text{SOC} \geq 60\%$  the intensity of region ② is almost 0 (Figure 4a,d). Considering this, we cannot only observe and quantitatively describe the color shift, but we are also able to correspond 30% SOC and 60% SOC with the onset of the  $\text{LiC}_{12}$  and  $\text{LiC}_6$  formation of the samples, as shown by the XRD results, where we found these onsets at 30% and 60% SOC.

When applying higher C-rates, we observed a heterogeneous lithiation with  $\text{LiC}_6$  forming already at low SOC in the images. This is also reflected by the colorimetric analysis. Figure 4b and c show the histograms for the hue values of electrodes charged to 30% SOC (Figure 4b) and 50% (Figure 4c) with C-rates up to 0.5C. The integrated peak maxima were again plotted against the SOC for all C-rates (Figure 4e). At 30% SOC, we observe a significant decrease in the intensity of region ② with increasing C-rate, indicating a decrease in the blue colored  $\text{LiC}_{18}$ . At 50% SOC, the intensity of region ① is growing remarkably with the C-rate, indicating the pronounced formation of  $\text{LiC}_6$ . As the region ② does not disappear completely, we can interpret a heterogeneous lithiation as implied by the qualitative analysis of the images.

Figure 5 shows the results of the segmentation of the different phases using ZEN Intellesis (left) and the evaluation of the phase fractions at different SOC (right).

In the segmented images, light blue was used to represent  $\text{LiC}_{18}$ , red was used to represent  $\text{LiC}_{12}$ , and yellow was used to represent  $\text{LiC}_6$ . The qualitative impressions of the segmentation results are in good agreement with the already described

color impressions from the microscopic images. The segmented images underline the generally inhomogeneous nature of the lithiation process. A more homogeneous surface is only produced (see Figure 5a) at SOC at the end of phase transitions 2L-2 (corresponding to 100 %  $\text{LiC}_{12}$ ) and 2-1 (corresponding to 100 %  $\text{LiC}_6$ ). The quantified phase proportions confirm the qualitative impression while charging with 0.1C to 30%–100% SOC and are shown in Figure 5a, right. At 30% SOC, the ratio of  $\text{LiC}_{18}$  to  $\text{LiC}_{12}$  is 87%/13%. With an increase up to 50% SOC, the  $\text{LiC}_{12}$  becomes dominant with a proportion of 85% whereas the  $\text{LiC}_{18}$  proportion drops close to zero, e.g., to 1% at 60% SOC. This is well in line with our colorimetric results, where we found that the intensity of the region ②, indicating  $\text{LiC}_{18}$ , dropped almost to 0. At this SOC, the onset of the  $\text{LiC}_6$  phase is detected and already accounts for 47%. The proportion of  $\text{LiC}_6$  phase increases continuously with higher SOC, up to 92% at 100% SOC, which correlates well with the results of the colorimetric measurements and with the increase in the range ① observed there.

As C-rates increase, surface color changes are visible (Figure 5b, left); surfaces turn redder at 30% SOC with fewer blue particles. Phase proportions align with color changes (Figure 5b, right), with the  $\text{LiC}_{12}$  phase growing from 13% at 0.1C to 59% at 0.5C. At 50% SOC, yellow particles emerge at 0.2C, while blue and red particles decline. The  $\text{LiC}_6$  phase fraction rises at 0.33C, but stagnates at 0.5C, while the  $\text{LiC}_{12}$  phase increases and the  $\text{LiC}_{18}$  decreases. This is well in line with the almost disappearing region ② in our colorimetric results and confirms the picture of heterogeneous lithiation.

In addition to quantitatively evaluating GIC-fractions, we were also able to quantify Li depositions on the surface of anodes by segmentation (Figure 6). A distinction was made between

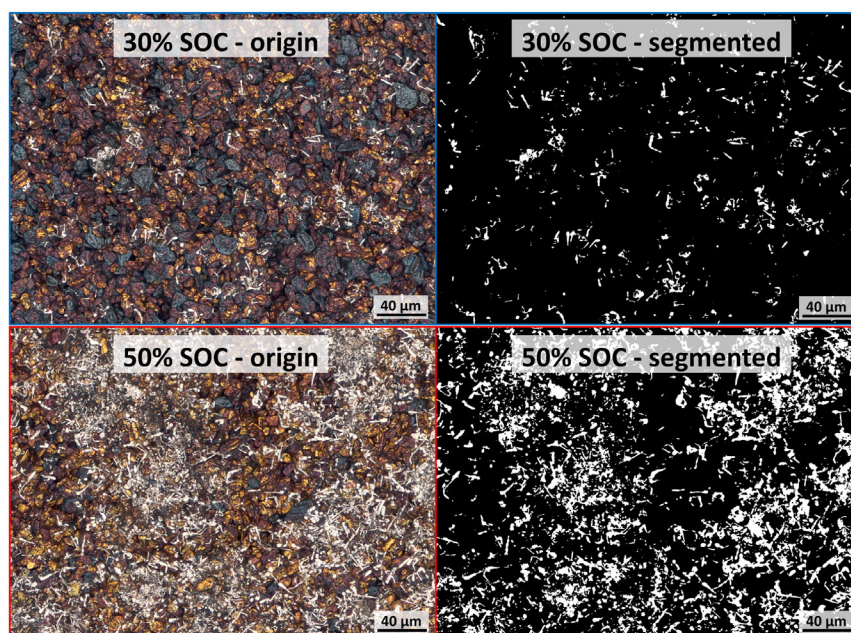


**Figure 6.** ML-based Li plating quantification using ZEN Intellesis. Anodes were charged with 1C to 30% SOC (top row) and 50% SOC (bottom row). Origin (left column) and segmented (right column) images are shown. A good separation between the unplated surface (black) and the Li deposition (white) is possible.

deposited Li (white segmented area) and the rest, which corresponds to different GICs (black segmented area). Segmented images show significantly more deposited Li on an anode surface charged to 50% SOC with 1C than for an anode charged to 30% SOC with 1C. In quantitative numbers, we found 4.15% and 32.5% of the surface covered with deposited Li for 30% SOC and 50% SOC, respectively. Note that with the microscopic top-view images, we are not able to get reliable information about the thickness of the deposited Li, and thus, a quantification of the total amount of Li plated is not possible.

### 3. Conclusion

In this work, high-resolution microscopy under an inert gas atmosphere was utilized to gain further insights into the lithiation and Li deposition mechanisms in graphite anodes for LIBs.

We were able to show that, unlike the visual impression of a homogeneous color we get from macro images of electrodes, at a microscopic scale, different lithiation stages are coexisting even within single particles, and even at low C-rates. At high C-rates, lithiation becomes more inhomogeneous and high Li stages such as  $\text{LiC}_6$  are locally visible already at a SOC of 30%. This indicates “hotspots” of lithiation, which most likely serve as nuclei for Li deposition. This effect is even more pronounced when charging the electrodes to 50% SOC.

As expected, Li deposition starts at a microscopic level with spot and needlelike deposits in the range of a few micrometers. The Li deposits can mostly be found on top of  $\text{LiC}_6$  particles, which supports the theory of high Li phases serving as nuclei for Li deposition. However, it cannot be ruled out that this visual appearance is partly affected by re-intercalation of deposited Li into the graphite.

The quality of the images significantly surpasses that of in situ optical studies and allows for colorimetric analysis and ML-based image segmentation to quantify the phases and their evolution. The results show a clear correlation between the hue value, the applied C-rate, and the achieved SOC.

The combination of high-resolution optical microscopy with ML-based and colorimetric analysis is an advantageous and powerful tool to investigate the lithiation of graphite and gain a comprehensive understanding of the influence of C-rate and SOC on the graphite lithiation and Li deposition behavior. Compared to XRD, glovebox optical microscopy provides a significantly higher spatial resolution. Additionally, optical microscopy focuses on where Li deposition starts and actually takes place, namely, the anode surface. XRD, in contrast, provides information that also comes from the bulk of the sample. However, the situation in the bulk is much less relevant to the question of Li deposition than the situation on the surface. This is also indicated by the electrochemical measurements. Although the electrode as a whole is still far below 100% SOC, we already find significant Li depositions on the surface since gradients in Li-concentration cannot be leveled fast enough.

With the described glovebox optical microscopy setup and workflow, we were able to establish a base for further studies to examine also the influence of electrode properties e.g., layer thickness and porosity, as well as materials properties such as graphite type or particle size.

### 4. Experimental Section

**Cell Setup and Electrochemical Tests:** The experiments were carried out using graphite anodes coated in ZSW's pilot line with an area capacity of  $3.1 \text{ mAh cm}^{-2}$ , a loading of  $8.7 \text{ mg cm}^{-2}$ , a porosity of  $42.4 \pm 0.3\%$  and a density of  $1.3 \text{ g cm}^{-3}$ . The anodes were also used in previous studies.<sup>[79–82]</sup> The anode properties are described in detail by Flügel et al.<sup>[80]</sup> The material manufacturer (Iopsilion, China) listed the specific capacity of the active material as  $355 \text{ mAh g}^{-1}$ .

All samples were dried in a drying oven at  $80^\circ\text{C}$  under air at ambient pressure for 12 h. The cell housing type CR2032 was used for all cell tests. Coin half cells were built in an Ar-filled glovebox ( $\text{GS}_2 < 0.5 \text{ ppm O}_2$  &  $< 0.5 \text{ ppm H}_2\text{O}$ ). Half-cell setup consists of a (graphite) anode  $\varnothing 12 \text{ mm}$  and a  $\varnothing 14 \text{ mm}$  Li foil (Sigma Aldrich,  $750 \mu\text{m}$  thickness), with a GF/A separator  $\varnothing 16 \text{ mm}$  (Whatmann plc) and Celgard 2325 (Celgard LLC) in between. The cells were filled with  $150 \mu\text{l}$   $1 \text{ M LiPF}_6$  in EC: DEC ( $3 : 7 \text{ wt.}\%$ ) +  $10 \text{ wt.}\%$  VC.

Half-cell testing was done with a BASYTEC CTS-Lab battery tester, and all cells were set in a climate chamber (Binder) at  $23^\circ\text{C}$ . The formation was carried out by cycling the cells three times between  $1.5 \text{ V}$  and  $10 \text{ mV}$  with a  $0.1\text{C}$  lithiation in constant current-constant voltage mode (CC-CV) with a termination criterion of  $< 0.025\text{C}$  and  $0.1\text{C}$  delithiation in CC mode. For the three formation cycles, charge and discharge currents were calculated using the electrode mass loading and the theoretical specific capacities given by the supplier. The discharge capacity of the third  $0.1\text{C}$  formation cycle is then defined as the rated capacity of the cell. That capacity is used to determine current rates for further cycling. For the subsequent investigations, the cells were lithiated (charged) in CC mode at different C-rates to different SOC.

**X-Ray Diffraction Experiments:** For XRD experiments, a GE Seifert Sun 3003 fast in situ XRD (XRD Eigenmann GmbH) with three Meteor1D detectors was used. Samples were prepared by gluing the washed and dried electrodes charged to the different SOC on a stainless-steel spacer and sealing them in a PP/PE-coated aluminum pouch foil bag with a  $25 \mu\text{m}$ -thick Kapton window. This bag protects the integrity of the sample over the time duration of the measurements up to several hours. Diffraction patterns were acquired between  $15^\circ$  and  $110^\circ$  ( $2\theta$ ) with steps of  $0.013^\circ$  ( $2\theta$ ) approximately utilizing Copper-K $\alpha$  radiation ( $\lambda = 1.5406 \text{ \AA}$ ) with the tube set to  $35 \text{ kV}$  and  $50 \text{ mA}$ .

**High-Resolution Light Microscopy: Sample Preparation and Image Acquisition:** The formatted cells were disassembled directly in an Ar-filled glovebox ( $\text{GS}_2 < 0.5 \text{ ppm O}_2$  &  $< 0.5 \text{ ppm H}_2\text{O}$ ) and the electrodes were washed with dimethyl carbonate (DMC). Transport to the glovebox and cell opening took less than 2 min.

Surface images of washed and dried anodes were taken with a ZEISS Axio Observer 7 with an EC Epiplan-Neofluar  $100\times/0.9 \text{ BD}$  objective using a neutral white (3200 K) LED and an extended depth of field mode inside the glovebox. The microscope was controlled completely from outside the GB, and images were always taken at a fixed sample position in the center of the electrode.

**Colorimetric Analysis Based on the Hue and Saturation Values:** We used ImageJ (Fiji)<sup>[83,84]</sup> for the procedure; however, this can be done by almost every image processing and analysis software, which is an additional advantage of our approach. For the analysis, the images were converted from the (RGB) red, green, blue color space into the (HSL) hue, saturation, luminance color space. Subsequently, the hue and saturation channels of the image were separated, and the histograms for each channel were calculated. Two distinct regions of the hue value were identified ( $0\text{--}30$  for region 1,  $135\text{--}165$  for region 2) and the mean value of each peak was calculated by integrating the peak height over the hue value.

**ML-Based Phase Analysis:** ZEN Intellesis was used for segmentation and phase analysis based on the original RGB images. This was done using pixel classification based on ML algorithms. We created a segmentation model using training data in the form of the images in this publication. During training, precise labeling and covering distinctive regions and especially boundaries for each phase were prioritized. The labeled pixels were then characterized by a feature vector of 50, and the model was used to segment single images.



## Supporting Information

Supporting Information is available from the Wiley Online Library or from the author.

## Acknowledgements

The authors gratefully acknowledge the support of the German Federal Ministry of Education and Research (BMBF) within the project CharLiSiKo (grant no. 03XP0333) as part of the AQua-Cluster. In addition, the authors want to thank Dr. Ute Golla-Schindler for providing the EDS Measurements with a windowless Bruker Extreme Detector at Aalen University. Publication funded by Aalen University of Applied Sciences.

Open Access funding enabled and organized by Projekt DEAL.

## Conflict of Interest

The authors declare no conflict of interest.

## Data Availability Statement

The data that support the findings of this study are available from the corresponding author upon reasonable request.

## Keywords

colorimetric analysis, high-resolution light microscopy, Li plating quantification, lithium-graphite intercalation phases, lithium-ion cells

Received: May 2, 2025

Revised: July 30, 2025

Published online:

- [1] J. B. Goodenough, K.-S. Park, *J. Am. Chem. Soc.* **2013**, *135*, 1167.
- [2] T. Waldmann, B.-I. Hogg, M. Wohlfahrt-Mehrens, *J. Power Sources* **2018**, *384*, 107.
- [3] X. Hu, L. Xu, X. Lin, M. Pecht, Battery Lifetime Prognostics, *Joule* **2020**, *4*, 310.
- [4] S. P. Rangarajan, Y. Barsukov, P. P. Mukherjee, *J. Mater. Chem. A* **2019**, *7*, 20683.
- [5] Y. Liu, Y. Zhu, Y. Cui, *Nat. Energy* **2019**, *4*, 540.
- [6] B. Ng, P. T. Coman, E. Faegh, X. Peng, S. G. Karakalos, X. Jin, W. E. Mustain, R. E. White, *Energy Mater.* **2020**, *3*, 3653.
- [7] T. Waldmann, J. B. Quinn, K. Richter, M. Kasper, A. Tost, A. Klein, M. Wohlfahrt-Mehrens, Post-Mortem Electrochemical, *J. Electrochem. Soc.* **2017**, *164*, A3154.
- [8] Q. Liu, C. Du, B. Shen, P. Zuo, X. Cheng, Y. Ma, G. Yin, Y. Gao, *RSC Adv.* **2016**, *6*, 88683.
- [9] R. V. Bugga, M. C. Smart, *ECS Trans.* **2010**, *25*, 241.
- [10] Z. Li, J. Huang, B. Yann Liaw, V. Metzler, J. Zhang, *J. Power Sources* **2014**, *254*, 168.
- [11] W. Lu, C. M. López, N. Liu, J. T. Vaughey, A. Jansen, W. Dennis, *J. Electrochem. Soc.* **2012**, *159*, A566.
- [12] J. R. Dahn, *Phys. Rev. B* **1991**, *44*, 9170.
- [13] M. Heß, P. Novák, *Electrochim. Acta* **2013**, *106*, 149.
- [14] D. Billaud, F. X. Henry, *Solid State Commun.* **2002**, *124*, 299.
- [15] J. Hattendorff, S. Seidlmayer, H. A. Gasteiger, R. Gilles, *J. Appl. Crystallogr.* **2020**, *53*, 210.
- [16] K. Richter, T. Waldmann, N. Paul, N. Jobst, R. Scurtu, M. Hofmann, R. Gilles, M. Wohlfahrt-Mehrens, *ChemSusChem* **2020**, *13*, 529.
- [17] V. Zinth, C. Von Lüders, J. Wilhelm, S. V. Erhard, M. Hofmann, S. Seidlmayer, J. Rebelo-Kornmeier, W. Gan, A. Jossen, R. Gilles, *J. Power Sources* **2017**, *361*, 54.
- [18] S. Migge, G. Sandmann, D. Rahner, H. Dietz, W. Plieth, *J. Solid State Electrochem.* **2005**, *9*, 132.
- [19] J.-C. Panitz, F. Joho, P. Novák, *Appl. Spectrosc.* **1999**, *53*, 1188.
- [20] R. Juza, V. Wehle, *Naturwissenschaften* **1965**, *52*, 560.
- [21] S. Konar, U. Häusserman, G. Svensson, *Chem. Mater.* **2015**, *27*, 2566.
- [22] A. Timmons, I. Hill, J. Dahn, *Meet. Abstr.* **2007**, MA2007-02, 755.
- [23] A. Ghannoum, R. C. Norris, K. Iyer, L. Zdravkova, A. Yu, P. Nieva, *ACS Appl. Mater. Interfaces* **2016**, *8*, 18763.
- [24] K. Nogami, H. Ueno, K. Yoshino, *J. Appl. Phys.* **1988**, *64*, 6460.
- [25] M. S. Dresselhaus, G. Dresselhaus, *Adv. Phys.* **2002**, *51*, 1.
- [26] P. Maire, A. Evans, H. Kaiser, W. Scheifele, P. Novák, *J. Electrochem. Soc.* **2008**, *155*, A862.
- [27] P. Maire, H. Kaiser, W. Scheifele, P. Novák, *J. Electroanal. Chem.* **2010**, *644*, 127.
- [28] S. J. Harris, A. Timmons, D. R. Baker, C. Monroe, *Chem. Phys. Lett.* **2010**, *485*, 265.
- [29] S. J. Harris, E. K. Rahani, V. B. Shenoy, *J. Electrochem. Soc.* **2012**, *159*, A1501.
- [30] B. Gyenes, D. A. Stevens, V. L. Chevrier, J. R. Dahn, *J. Electrochem. Soc.* **2015**, *162*, A278.
- [31] F. Grimsman, T. Gerbert, F. Brauchle, A. Gruhle, J. Parisi, M. Knipper, *J. Energy Storage* **2018**, *15*, 17.
- [32] C. Hogrefe, T. Waldmann, M. B. Molinero, L. Wildner, P. Axmann, M. Wohlfahrt-Mehrens, *J. Electrochem. Soc.* **2022**, *169*, 050519.
- [33] C. Hogrefe, T. Waldmann, M. Hölzle, M. Wohlfahrt-Mehrens, *J. Power Sources* **2023**, *556*, 232391.
- [34] K. E. Thomas-Alyea, C. Jung, R. B. Smith, M. Z. Bazant, *J. Electrochem. Soc.* **2017**, *164*, E3063.
- [35] A. Jansche, S. Desapogu, C. Hogrefe, A. K. Choudhary, F. Trier, A. Kopp, C. Weisenberger, T. Waldmann, M. Wohlfahrt-Mehrens, T. Bernthaler, G. Schneider, *Pract. Metallogr.* **2023**, *60*, 148.
- [36] S. Agrawal, P. Bai, *Science* **2022**, *3*, 100854.
- [37] D. Fraggadakis, N. Nadkarni, T. Gao, T. Zhou, Y. Zhang, Y. Han, R. M. Stephens, Y. Shao-Horn, M. Z. Bazant, *Energy Environ. Sci.* **2020**, *13*, 2142.
- [38] T. Gao, Y. Han, D. Fraggadakis, S. Das, T. Zhou, C.-N. Yeh, S. Xu, W. C. Chueh, J. Li, M. Z. Bazant, *Joule* **2021**, *5*, 393.
- [39] C. Fear, T. Adhikary, R. Carter, A. N. Mistry, C. T. Love, P. P. Mukherjee, *ACS Appl. Mater. Interfaces* **2020**, *12*, 30438.
- [40] S. P. Rangarajan, C. Fear, T. Adhikary, Y. Barsukov, G. Dadheech, P. P. Mukherjee, *Science* **2023**, *4*, 101740.
- [41] R. L. Sacci, L. W. Gill, E. W. Hagaman, N. J. Dudney, *J. Power Sources* **2015**, *287*, 253.
- [42] V. Badrinarayanan, A. Kendall, R. Cipolla, *IEEE Trans. Pattern Anal. Mach. Intell.* **2017**, *39*, 2481.
- [43] D. Mahapatra, *IEEE Trans. on Image Process.* **2014**, *23*, 1504.
- [44] S. Müller, C. Sauter, R. Shunmugasundaram, N. Wenzler, V. De Andrade, F. De Carlo, E. Konukoglu, V. Wood, *Nat. Commun.* **2021**, *12*, 6205.
- [45] J. J. Bailey, A. Wade, A. M. Boyce, Y. S. Zhang, D. J. L. Brett, P. R. Shearing, *J. Power Sources* **2023**, *557*, 232503.
- [46] K. P. C. Yao, J. S. Okasinski, K. Kalaga, J. D. Almer, D. P. Abraham, *Adv. Energy Mater.* **2019**, *9*, 1803380.
- [47] M. Inaba, H. Yoshida, Z. Ogumi, T. Abe, Y. Mizutani, M. Asano, *J. Electrochem. Soc.* **1995**, *142*, 20.
- [48] T. Tran, K. Kinoshita, *J. Electroanal. Chem.* **1995**, *386*, 221.
- [49] F. Yao, F. Güneş, H. Q. Ta, S. M. Lee, S. J. Chae, K. Y. Sheem, C. S. Cojocaru, S. S. Xie, Y. H. Lee, *J. Am. Chem. Soc.* **2012**, *134*, 8646.
- [50] S. J. Harris, P. Lu, *J. Phys. Chem. C* **2013**, *117*, 6481.

- [51] D. E. Stephenson, E. M. Hartman, J. N. Harb, D. R. Wheeler, *J. Electrochem. Soc.* **2007**, *154*, A1146.
- [52] M. Smith, R. E. García, Q. C. Horn, *J. Electrochem. Soc.* **2009**, *156*, A896.
- [53] C. Hogrefe, M. Hölzle, M. Wohlfahrt-Mehrens, T. Waldmann, *J. Electrochem. Soc.* **2023**, *170*, 110535.
- [54] P. Arora, M. Doyle, R. E. White, *J. Electrochem. Soc.* **1999**, *146*, 3543.
- [55] S. Hein, T. Danner, A. Latz, *Energy Mater.* **2020**, *3*, 8519.
- [56] X. Lu, M. Lagnoni, A. Bertei, S. Das, R. E. Owen, Q. Li, K. O'Regan, A. Wade, D. P. Finegan, E. Kendrick, M. Z. Bazant, D. J. L. Brett, P. R. Shearing, *Nat. Commun.* **2023**, *14*, 5127.
- [57] M. Bauer, B. Rieger, S. Schindler, P. Keil, M. Wachtler, M. A. Danzer, A. Jossen, *J. Energy Storage* **2017**, *10*, 1.
- [58] N. Sharma, V. K. Peterson, *Electrochim. Acta* **2013**, *101*, 79.
- [59] C. Uhlmann, J. Illig, M. Ender, R. Schuster, E. Ivers-Tiffée, *J. Power Sources* **2015**, *279*, 428.
- [60] N. Legrand, B. Knosp, P. Desprez, F. Lapique, S. Raël, *J. Power Sources* **2014**, *245*, 208.
- [61] M. D. Levi, E. Markevich, D. Aurbach, *J. Phys. Chem. B* **2005**, *109*, 7420.
- [62] K. Xu, *J. Electrochem. Soc.* **2007**, *154*, A162.
- [63] Y. Chen, K.-H. Chen, A. J. Sanchez, E. Kazyak, V. Goel, Y. Gorlin, J. Christensen, K. Thornton, N. P. Dasgupta, *J. Mater. Chem. A* **2021**, *9*, 23522.
- [64] C. Hogrefe, S. Hein, T. Waldmann, T. Danner, K. Richter, A. Latz, M. Wohlfahrt-Mehrens, *J. Electrochem. Soc.* **2020**, *167*, 140546.
- [65] O. Bayindir, I. H. Sohel, M. Erol, Ö. Duygulu, M. N. Ateş, *ACS Appl. Mater. Interfaces* **2022**, *14*, 891.
- [66] K. Zaghib, G. Nadeau, K. Kinoshita, *J. Power Sources* **2001**, *97–98*, 97.
- [67] J. P. Olivier, M. Winter, *J. Power Sources* **2001**, *97–98*, 151.
- [68] Y. Yamada, K. Miyazaki, T. Abe, *Langmuir* **2010**, *26*, 14990.
- [69] M. Mundsinger, S. Farsi, M. Rapp, U. Golla-Schindler, U. Kaiser, M. Wachtler, *Carbon* **2017**, *111*, 764.
- [70] S. Malifarge, B. Delobel, C. Delacourt, *J. Power Sources* **2017**, *343*, 338.
- [71] T. Nishida, K. Nishikawa, M. Rosso, Y. Fukunaka, *Electrochim. Acta* **2013**, *100*, 333.
- [72] M. Sadd, S. Xiong, J. R. Bowen, F. Marone, A. Matic, *Nat. Commun.* **2023**, *14*, 854.
- [73] J. Steiger, D. Kramer, R. Mönig, *Electrochim. Acta* **2014**, *136*, 529.
- [74] S. Perumaram Rangarajan, Y. Barsukov, P. P. Mukherjee, *Science* **2022**, *3*, 100720.
- [75] R. Carter, T. A. Kingston, R. W. Atkinson, M. Parmananda, M. Dubarry, C. Fear, P. P. Mukherjee, C. T. Love, *Science* **2021**, *2*, 100351.
- [76] T. Waldmann, B.-I. Hogg, M. Kasper, S. Grolleau, C. G. Couceiro, K. Trad, B. P. Matadi, M. Wohlfahrt-Mehrens, *J. Electrochem. Soc.* **2016**, *163*, A1232.
- [77] M. C. Smart, R. V. Bugga, *J. Electrochem. Soc.* **2011**, *158*, A379.
- [78] A. Klein, M. Sadd, N. Mozghukhina, M. Olsson, L. Broche, S. Xiong, A. Matic, *Batteries Amp. Supercaps* **2024**, *7*, e202400070.
- [79] M. Flügel, K. Richter, M. Wohlfahrt-Mehrens, T. Waldmann, *J. Electrochem. Soc.* **2022**, *169*, 050533.
- [80] M. Flügel, M. Bolsinger, M. Marinaro, V. Knoblauch, M. Hölzle, M. Wohlfahrt-Mehrens, T. Waldmann, *J. Electrochem. Soc.* **2023**, *170*, 060536.
- [81] K. Bischof, M. Flügel, M. Hölzle, M. Wohlfahrt-Mehrens, T. Waldmann, *J. Electrochem. Soc.* **2024**, *171*, 010510.
- [82] C. Hogrefe, N. Paul, L. Boveleth, M. Bolsinger, M. Flügel, T. Danner, A. Latz, R. Gilles, V. Knoblauch, M. Wohlfahrt-Mehrens, M. Hölzle, T. Waldmann, *J. Electrochem. Soc.* **2024**, *171*, 070503.
- [83] J. Schindelin, I. Arganda-Carreras, E. Frise, V. Kaynig, M. Longair, T. Pietzsch, S. Preibisch, C. Rueden, S. Saalfeld, B. Schmid, J.-Y. Tinevez, D. J. White, V. Hartenstein, K. Eliceiri, P. Tomancak, A. Cardona, *Nat Methods* **2012**, *9*, 676.
- [84] C. A. Schneider, W. S. Rasband, K. W. Eliceiri, *Nat Methods* **2012**, *9*, 671.